

Observing quantum many-body dynamics in emergent curved spacetime using programmable quantum processors

Brendan Rhyno,^{1, 2, *} Bastien Lapierre,^{3, 4, *} Smitha

Vishveshwara,¹ Khadijeh Najafi,^{5, 6} and Ramasubramanian Chitra⁷

¹*Department of Physics, University of Illinois at Urbana-Champaign, Urbana, Illinois 61801, USA*

²*Institute of Quantum Optics, Leibniz Universität Hannover, Welfengarten 1, 30167 Hannover, Germany*

³*Department of Physics, Princeton University, Princeton, New Jersey, 08544, USA*

⁴*Philippe Meyer Institute, Physics Department, École Normale Supérieure (ENS), Université PSL, 24 rue Lhomond, F-75231 Paris, France*

⁵*IBM Quantum, IBM T.J. Watson Research Center, Yorktown Heights, 10598, USA*

⁶*MIT-IBM Watson AI Lab, Cambridge MA, 02142, USA*

⁷*Institute for Theoretical Physics, ETH Zurich, Wolfgang-Pauli-Str. 27, CH-8093 Zurich, Switzerland*

(Dated: February 18, 2026)

We digitally simulate quantum many-body dynamics in emergent curved backgrounds using 80 superconducting qubits on IBM Heron processors. By engineering spatially varying couplings in the spin- $\frac{1}{2}$ XXZ chain, consistent with the low energy description of the model in terms of an inhomogeneous Tomonaga-Luttinger liquid, we realize excitations that follow geodesics of an effective metric inherited from the underlying spatial deformation. Following quenches from Néel and few-spin-flip states, we observe curved light-cone propagation, horizon-induced freezing in the local magnetization, and position-dependent oscillation frequencies set by the engineered spatial deformation. Despite strong spatial inhomogeneity, unequal-time correlators reveal ballistic quasiparticle propagation in the spin chain. These results establish large-scale digital quantum processors as a flexible platform for detailed and controlled exploration of many-body dynamics in tunable and synthetic curved spacetimes.

Introduction. The current day description of gravitation and cosmology hinges on curved spacetime. Against this backdrop, the full-fledged physics of black holes and the early universe relies on the coupling between geometry and quantum fields. W. G. Unruh's seminal work [1] unveiled the possibility of simulating field theories in curved spacetime using tabletop experiments, thereby paving the way for controlled studies of the interplay between spacetime curvature and quantum matter. These insights have spurred experimental realizations of curved spacetime analogs in both classical and quantum fluids in a range of systems [2–13]. Here we present large-scale digital quantum processors as a fertile arena for realizing quantum dynamics in emergent curved backgrounds.

Our key guiding principle is as follows: A central feature of spacetime is its causal structure, manifested in light-cones that set bounds on the propagation of physical information. In relativistic theories, such a bound is fundamentally set by the speed of light. In nonrelativistic quantum many-body lattice systems, the propagation of correlations is limited by the Lieb-Robinson bound [14]. Quite generally, a broad class of quantum systems at criticality exhibit an emergent Lorentz invariance at large distances, so that their low-energy dynamics is governed by relativistic quantum field theories in flat spacetime with effective speeds of light. In one spatial dimension, these theories are universal and conform to the paradigm of Tomonaga-Luttinger liquids (TLLs) [15]. The predicted light-cone-like propagation of quantum information [16, 17] has been observed in ultracold atom experiments [18–21]. In recent years, superconducting

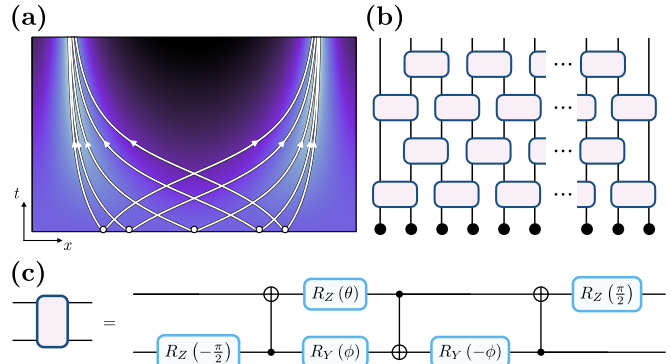


Figure 1. **Simulating spatially inhomogeneous dynamics with quantum processors.** (a) In our inhomogeneous quench protocol, the initial state acts as a source of pairs of quasiparticles (illustrated as white dots), which propagate along geodesics on a curved background. (b) Quantum circuit implementation of the time evolution operator $\exp(-i\delta t H)$ for the deformed XXZ spin chain, Eq. (2), using a first-order Suzuki-Trotter decomposition with a time step of duration δt . Each Trotter layer consists of an “odd” and “even” sublayer composed of unitaries that couple nearest-neighbour qubits. (c) The corresponding two qubit quantum circuit; here the rotation gate angles are $\theta = 2\delta t v_j \Delta + \pi/2$ and $\phi = -2\delta t v_j - \pi/2$ encoding both local interactions through the anisotropy Δ and emergent spacetime curvature through the deformation profile v_j .

quantum processors have also emerged as a promising complementary route for simulating the physics of quantum fields in curved spacetime [22–25]. Digital quantum

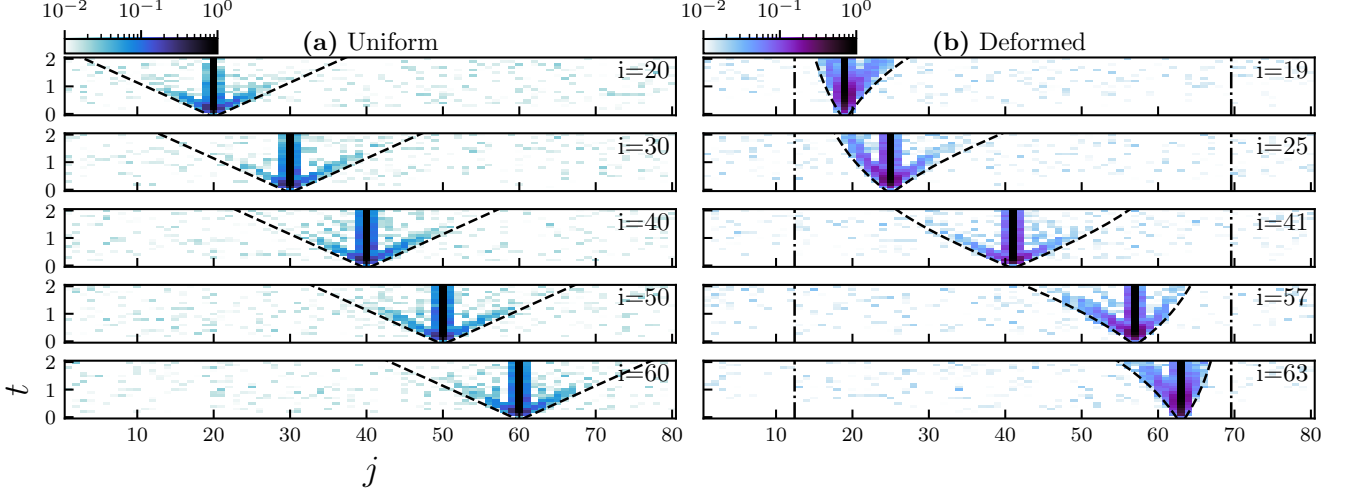


Figure 2. Curved light-cone propagation. Light-cone propagation in the two-point correlation function $|C_{ij}^{zz}(t)|$ following a quench with (2) from an initial Néel state in an interacting chain of $N = 80$ qubits. (a) Uniform XXZ chain simulated on `ibm_fez` with $\Delta = 1/2$. (b) Deformed XXZ chain simulated on `ibm_marrakesh` with the same anisotropy ($\Delta = 1/2$) and a deformation given by (4), with Rindler horizons located at $j_* + 1$ and $N + 1 - j_*$ with $j_* = N/7$ (indicated with black dash-dot vertical lines). The observed light cones are compared to the geodesics of the metric (1) (black dashed curves) for various initial positions i , computed using $\frac{1}{8} \int_i^j dx v(x)^{-1}$. Color maps share a common logarithmic scale, with the lower bound set by the order of magnitude associated with the standard error in each observable.

simulations of large many-body systems offer advantages due to their high degree of tunability [26–33], which enables near arbitrary control of the spatial and temporal structure of the effective curved background metric.

In this work, we simulate quantum many-body dynamics in a curved background, leveraging the superconducting transmon-qubit architecture of IBM Heron processors. Unlike analog quantum simulators, this digital platform provides fine-grained control over the effective spacetime metric, enabling the programmable realization of curved geometries with emergent horizons, and allowing a systematic exploration of their consequences for quantum dynamics. As a concrete demonstration, we study the nonequilibrium evolution of a spatially deformed one-dimensional interacting quantum spin chain, where the deformation provides a lever to tune local spacetime metric. The high tunability of quantum gates allows us to access a wide range of spatial deformations and interaction strengths, spanning both gapless and gapped phases. Using chains of 80 qubits, we observe deformed light-cone propagation in the gapless regime, consistent with the long-wavelength description of the spin chain as a TLL in a curved spacetime with metric

$$ds^2 = dx^2 - v(x)^2 dt^2. \quad (1)$$

Strikingly, these results are obtained with only minimal error mitigation, and the relevant dynamical signatures remain clearly visible for up to 20 Trotter steps, highlighting the robustness of digital quantum processors in simulating curved geometries.

Setup. To simulate quantum many-body dynamics in a curved background, we consider a spatially deformed version of the paradigmatic spin- $\frac{1}{2}$ XXZ chain [we set $J = \hbar = 1$ thereafter],

$$H = J \sum_{j=1}^{N-1} v_j [\sigma_j^x \sigma_{j+1}^x + \sigma_j^y \sigma_{j+1}^y + \Delta \sigma_j^z \sigma_{j+1}^z], \quad (2)$$

where the deformation profile v_j is assumed to vary smoothly over mesoscopic length scales much larger than the lattice spacing. As in the homogeneous case, for smooth deformations, the model is gapless for $|\Delta| < 1$ and gapped otherwise [34]. Using bosonization, it can be seen that the gapless regime lends itself to a low-energy effective description of (2) in terms of an *inhomogeneous* TLL [21, 34–38]

$$H_{\text{TLL}}[v] = \int_0^L dx \frac{v(x)}{2\pi} \left[\frac{1}{K} (\partial_x \varphi(x))^2 + K (\partial_x \theta(x))^2 \right], \quad (3)$$

for the dual bosonic fields $\varphi(x)$ and $\theta(x)$, and Luttinger parameter K [39]. The factor $v(x)$ can be absorbed in the spacetime metric through a conformal transformation, leading to a theory in curved spacetime with metric (1) [34, 35, 40]. Therefore, low-energy gapless excitations in the spin chain (2) with $|\Delta| < 1$, which consist of left- and right-moving modes, follow lightlike geodesics, as given by $ds^2 = 0$. In the following, we consider the deformation profile

$$v_j = \frac{\sin\left(\frac{\pi}{N}(j-1-j_*)\right) \sin\left(\frac{\pi}{N}(j-1+j_*)\right)}{\sin\left(\frac{2\pi}{N}j_*\right)}. \quad (4)$$

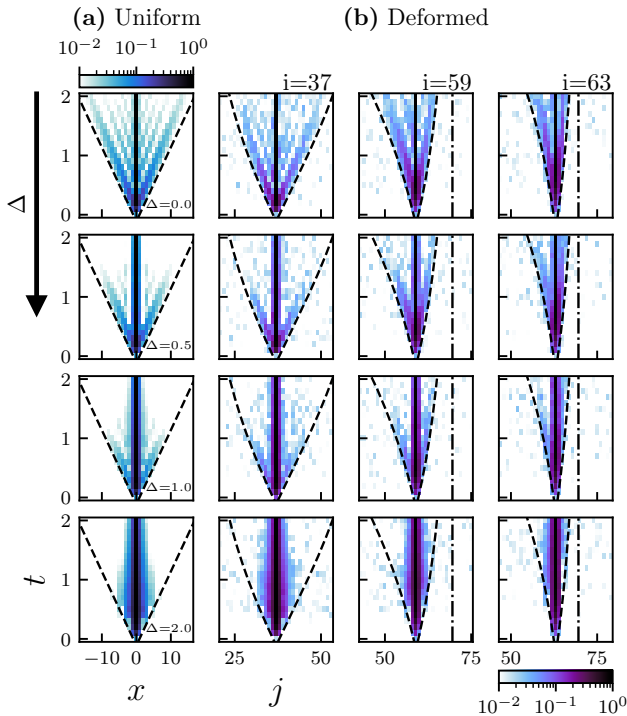


Figure 3. Tuning interactions. (a) Spatially averaged two-point correlator $|C^{zz}(x, t)| = |\frac{1}{N_x} \sum_i C_{i,i+x}^{zz}(t)|$, where N_x is the number of pairs of sites separated by distance $|x|$ [48], following a quench with the uniform XXZ chain initialized in a Néel state using several interaction strengths, $\Delta = 0, 1/2, 1$, and 2 . (b) Correlation function $|C_{ij}^{zz}(t)|$ following a quench with the inhomogeneous XXZ chain (same deformation as in Fig. 2(b)) for different positions, $i = 37, 59, 63$, using the same initial state and Δ values as in (a). All quantum simulations here were performed on `ibm_fez`.

With this choice of deformation, the resulting spacetime metric (1) features two emergent Rindler horizons around sites $j_* + 1$ and $N + 1 - j_*$, where the velocity approaches zero linearly. Consequently, between the two horizons, every chiral (antichiral) gapless quasiparticle accumulates at the site nearest to $j_* + 1$ ($N + 1 - j_*$), which leads to a localization of all quantum entanglement at the two horizons [41]. The resulting deformed Hamiltonian admits a natural interpretation as the entanglement Hamiltonian in (1+1)d conformal field theory [42, 43], and can be also be realized as an effective Hamiltonian via Floquet engineering [41, 44, 45]. Note that all quasiparticles (and hence energy) accumulate at the two horizons with time. This can be interpreted as an effective cooling of the bulk and can be harnessed as a route towards efficient ground state preparation [46, 47].

Our nonequilibrium protocol is an inhomogeneous variant of the paradigmatic global quantum quench [49]: we initialize the system in a massive state $|\Psi_0\rangle$, and extract the time evolution of observables after quenching with the gapless deformed XXZ model (2). At $t = 0$, pairs of exci-

tations with opposite chirality are created at all positions and propagate according to geodesics of the metric (1). In the following, (i) we experimentally extract signatures of the curved metric (1), and (ii) we demonstrate the ballistic nature of the excitations of (2), confirming that the dynamics of such an inhomogeneous interacting spin chain is governed by gapless quasiparticles.

Curved light-cone propagation. As a direct probe of the effective curved metric generated by the spatially dependent spin coupling in (2), we simulate the equal-time connected spin-spin correlation function, defined as

$$C_{ij}^{zz}(t) = \langle \sigma_i^z(t) \sigma_j^z(t) \rangle - \langle \sigma_i^z(t) \rangle \langle \sigma_j^z(t) \rangle, \quad (5)$$

starting from an initial Néel state $|\Psi_0\rangle = |\uparrow\downarrow\uparrow\downarrow\ldots\rangle$. This choice has two advantages: it circumvents the challenging problem of preparing the critical ground state, and, more importantly, as the time evolution is fundamentally dictated by the low-energy spinons stemming from domain wall formation, it directly probes the effective Luttinger theory. Working in the Schrödinger picture, the initial state time evolves as $|\Psi(t)\rangle = e^{-itH} |\Psi_0\rangle$, where the time evolution operator is achieved by a first-order Suzuki-Trotter decomposition using time steps of duration $\delta t = 0.1$ (see Supplementary Material (SM) [50] for details and references [27, 51, 52]). After initial state preparation and applying gate implementations of the Trotterized unitary to reach the $s = 0, 1, 2, \dots, 20$ Trotter step, the system is measured along the z -axis (computational basis), and this process is repeated many times. Here, we use 2^{14} measurement shots, which results in a standard error in the correlation functions on the order of 10^{-2} . These quantum simulations were carried out on the IBM Heron processors `ibm_fez` and `ibm_marrakesh`, using the Qiskit Runtime Sampler primitive. Circuit layouts were compiled with level-3 transpiler optimization, and Pauli twirling together with dynamical decoupling were applied as low-cost error mitigation and suppression techniques.

The results for the correlator (5) are displayed in Fig. 2(a) for a uniform XXZ chain, and Fig. 2(b) for the inhomogeneous chain; the latter are explicitly compared with the lightlike geodesics of the metric (1), showing excellent agreement. Our results confirm that the light-cone structure is strongly sensitive to the location of the initial excitation in the deformed setting. Notably, a clear left-right asymmetry emerges as the excitations approach the Rindler horizons generated by the deformation (4). We emphasize that, although decoherence in quantum processors prevents us from accessing times at which gapless quasiparticles traverse the full system, simulating sufficiently large system sizes N is nonetheless essential. Only then do the couplings in Eq. (2) vary slowly enough relative to the lattice spacing for the low-energy dynamics to admit an emergent field-theoretic description in curved spacetime.

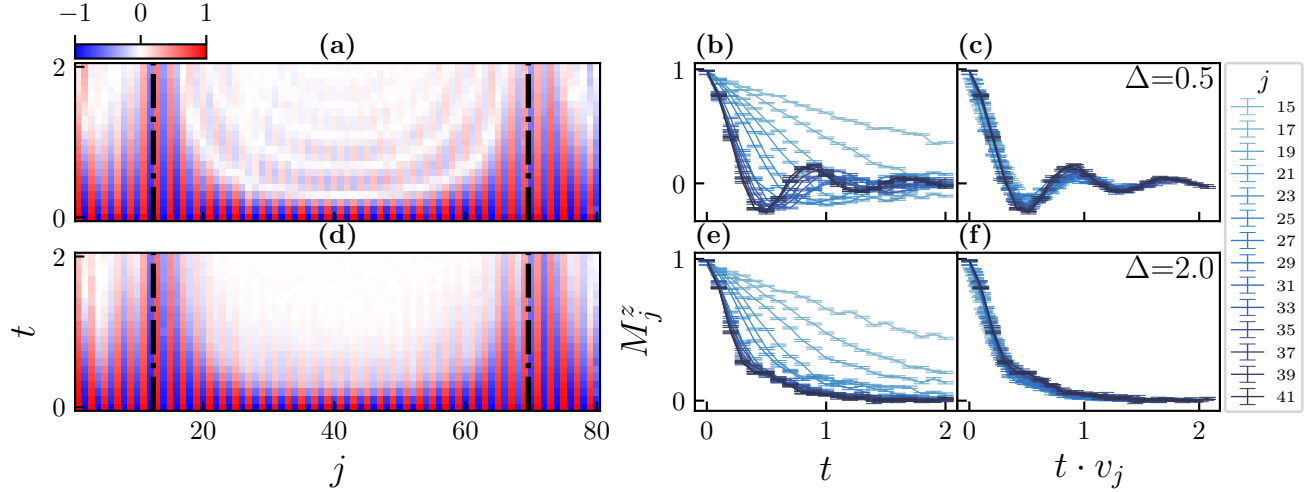


Figure 4. Magnetization dynamics. (a) Time evolution of the local magnetization $M_j^z(t)$ from an initial Néel state, for the same parameters as Fig. 3(b). The effective curved spacetime given by the metric (1) manifests as inhomogeneous oscillation periods that freeze at the horizons (denoted by black dash-dot vertical lines). (b) Damped oscillations at different initial positions reveal a strong position dependence of the frequency. (c) Collapse of the magnetization curves after rescaling the time axis by the spatial deformation. Standard errors in each measurement have been included. (d-f) Corresponding results in the gapped phase ($\Delta = 2$), where oscillations are suppressed.

To probe how interactions affect the curved light-cone structure, we simulated the inhomogeneous XXZ chain across different anisotropy values Δ spanning both critical and gapped regimes; the corresponding results are displayed in Fig. 3. Clear resonances manifest within the light cones, consistent with coherent free propagation in the noninteracting case ($\Delta = 0$). The light cones remain stable as we tune Δ through the gapless regime. In the gapped phase ($\Delta = 2$), we observe a local deformation-dependent exponential suppression of propagation.

Magnetization as a probe of local curvature. For the uniform XXZ model in the gapless regime, it has been demonstrated that the dynamics of the magnetization starting from a Néel state shows damped Rabi-like oscillations, with frequency set by the exchange coupling J . Importantly, these oscillations lie beyond the TLL description [53, 54], reflecting their non-universal, lattice-scale origin. It is therefore natural to ask whether such oscillations are affected by the effective metric (1). We demonstrate that this is the case by studying the time dependence of the local magnetization $M_j^z(t) = \langle \sigma_j^z(t) \rangle$ after an inhomogeneous quench with (2), starting from the Néel state. While the absence of translational invariance would in general preclude any nontrivial structure of the magnetization beyond exponential decay, the smooth inhomogeneity in (2) leads to intriguing dynamics. In fact, as we show in the SM [50] for the noninteracting case $\Delta = 0$, $M_j^z(t)$ showcases robust oscillations, similar to the homogeneous case, but with an explicitly spatially dependent frequency $\omega_j \propto J|v_j|$. A direct consequence of this relation is that the local magnetization freezes near

the horizons, accompanied by a divergence in the decay time. In other words, the memory of the initial state is kept for parametrically long times when approaching the horizons.

We confirm the emergence of this spatially dependent dynamics in the magnetization $M_j^z(t)$ for $|\Delta| < 1$, as shown in Fig. 4(a–c). Focusing on $\Delta = 1/2$, we measure $M_j^z(t)$ for an initial Néel state and observe the expected damped oscillations, whose frequency varies with position in the gapless regime. As demonstrated in Fig. 4(c), these curves collapse onto a single universal profile once the time axis is rescaled by the spatial deformation v_j . This implies that oscillations of the magnetization directly probes the local velocity (1). Remarkably, our results indicate that the effective metric governs the observable dynamics even beyond the continuum regime.

In contrast, in the gapped regime with $\Delta = 2$, we observe that the local magnetization does not exhibit oscillations, as shown in Fig. 4(d–e). Nevertheless, even for $\Delta = 2$, the magnetization remains spatially modulated by the deformation, and the decay rate is parametrically reduced near the horizons. Remarkably, the magnetization decay curves show an almost perfect collapse once time is rescaled by the spatial deformation, as shown in Fig. 4(f).

Signatures of ballistic transport. In the absence of inhomogeneity, the XXZ model is integrable and exhibits ballistic transport for $|\Delta| < 1$ [55]. Although generic deformations of the XXZ model break integrability and typically lead to diffusive transport [56], the spin chain (2) remains ballistic and is described in the low-

energy regime by a TLL on a curved background. We now test the ballistic nature of our model by studying the propagation of quasiparticles from the unequal time correlator $G_{ji}^{zz}(t, 0) = \langle \sigma_j^z(t) \sigma_i^z(0) \rangle$. The initial states we consider in the following are of the form

$$|j_1, j_2, \dots, j_n\rangle = \prod_{a=1}^n \sigma_{j_a}^x |\uparrow \dots \uparrow\rangle, \quad (6)$$

where the spins at the sites j_1, j_2, \dots, j_n are down, with the rest being up. We consider two distinct protocols: one where the initial state consists of a double spin-flip, i.e. $|j_1, j_2\rangle$, and another with single spin-flip states of the form $|j_1\rangle$ and $|j_2\rangle$. For these initial states, the unequal-time spin-spin correlator is related to the local magnetization by $G_{ji}^{zz}(t, 0) = M_j^z(t) M_i^z(0)$. In the case of a uniform XXZ chain, we find that the unequal-time correlator is nearly identical between both initial state choices, as shown in Fig. 5(a-b). This independence of the ini-

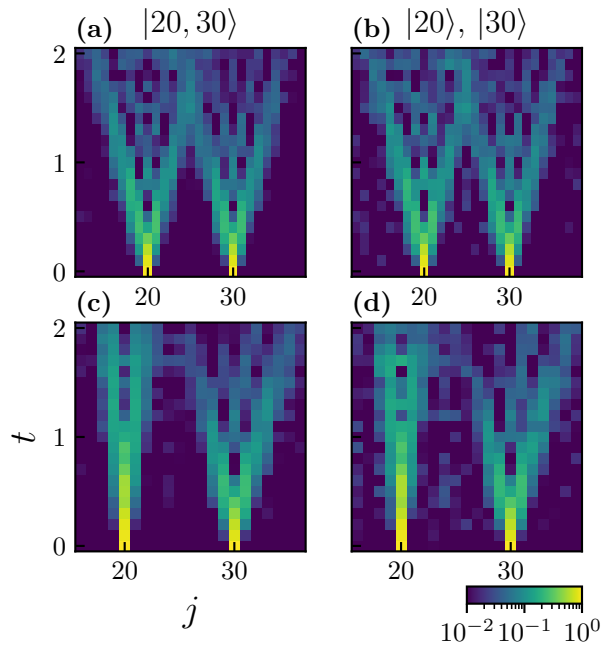


Figure 5. Ballistic spreading of correlations. Panels (a) and (c) show $N = 80$ qubit simulation results of the unequal-time correlation function for a uniform chain and a deformed chain ($\Delta = 1/2$), respectively, when the initial state contains two spin flips located at sites 20 and 30. Panels (b) and (d) instead compare the dynamics starting from a single spin flip: we prepare one state with the flip at site 20 and another at site 30, compute the corresponding correlation functions, and overlay the results for direct comparison with the two-spin flip state. In all cases we have subtracted off the background magnetization by performing simulations with an initial all-up spin state.

tial state is a clear signature of ballistic transport in the gapless chain. For the deformed XXZ chain, we similarly observe independence from the initial spin flips; see

Fig. 5(c-d). Due to the strong effects of the deformation, the quasiparticles emitted at positions 20 and 30 do not significantly overlap on the simulable timescale.

Outlook. Our successful demonstration of critical quantum dynamics in a curved background using digital simulators heralds exciting future prospects. By changing the connectivity of our qubit graph, our work can be extended to two dimensions in a straightforward manner. The ease of imprinting time dependent metrics in these platforms is of direct relevance to quantum simulations of cosmological phenomena such as inflationary particle production and density fluctuations [57–63], analog black holes [1, 64–67], and other realms of analog gravity [68, 69]. Beyond the direct simulation of quantum field theories, these simulators offer a platform to investigate fundamental questions, such as the emergence of inhomogeneous butterfly velocity in out-of-time-order correlators [31, 70–73] and Kardar–Parisi–Zhang (KPZ) scaling from noisy spatiotemporal deformations [52, 74]. A promising future direction is the coupling of the original metric to the quantum evolution of matter via backreaction feedback to update inhomogeneities of the system. This permits the simulation of toy models of gravity [75] and to test if horizons emerge dynamically from backreaction [76, 77].

Acknowledgments. B.L. acknowledges financial support from the Swiss National Science Foundation (Post-doc.Mobility Grant No. 214461). B.R. acknowledges the support of the Quantum Leap Challenge Institute for Hybrid Quantum Architectures and Networks Grant No. OMA2016136. S.V. acknowledges the support of the National Science Foundation through Grant No. DMR2004825. We acknowledge the use of IBM Quantum Credits for this work. The views expressed are those of the authors, and do not reflect the official policy or position of IBM or the IBM Quantum team.

Competing Interests. The authors declare no competing interests.

* These authors contributed equally to this work.

- [1] W. G. Unruh, “Experimental Black-Hole Evaporation?” *Phys. Rev. Lett.* **46**, 1351–1353 (1981).
- [2] Oren Lahav, Amir Itah, Alex Blumkin, Carmit Gordon, Shahar Rinott, Alona Zayats, and Jeff Steinhauer, “Realization of a Sonic Black Hole Analog in a Bose-Einstein Condensate,” *Phys. Rev. Lett.* **105**, 240401 (2010).
- [3] Silke Weinfurter, Edmund W. Tedford, Matthew C. J. Penrice, William G. Unruh, and Gregory A. Lawrence, “Measurement of Stimulated Hawking Emission in an Analogue System,” *Phys. Rev. Lett.* **106**, 021302 (2011).
- [4] Jeff Steinhauer, “Observation of self-amplifying Hawking radiation in an analogue black-hole laser,” *Nature Physics* **10**, 864–869 (2014).
- [5] S. Eckel, A. Kumar, T. Jacobson, I. B. Spielman, and G. K. Campbell, “A Rapidly Expanding Bose-Einstein

Condensate: An Expanding Universe in the Lab," *Phys. Rev. X* **8**, 021021 (2018).

[6] Jiazhong Hu, Lei Feng, Zhendong Zhang, and Cheng Chin, "Quantum simulation of Unruh radiation," *Nature Physics* **15**, 785–789 (2019).

[7] Juan Ramón Muñoz de Nova, Katrine Golubkov, Victor I. Kolobov, and Jeff Steinhauer, "Observation of thermal Hawking radiation and its temperature in an analogue black hole," *Nature* **569**, 688–691 (2019).

[8] Matthias Wittemer, Frederick Hakelberg, Philip Kiefer, Jan-Philipp Schröder, Christian Fey, Ralf Schützhold, Ulrich Warring, and Tobias Schaetz, "Phonon Pair Creation by Inflating Quantum Fluctuations in an Ion Trap," *Phys. Rev. Lett.* **123**, 180502 (2019).

[9] Theo Torres, Sam Patrick, Maurício Richartz, and Silke Weinfurtner, "Quasinormal Mode Oscillations in an Analogue Black Hole Experiment," *Phys. Rev. Lett.* **125**, 011301 (2020).

[10] S. Banik, M. Gutierrez Galan, H. Sosa-Martinez, M. J. Anderson, S. Eckel, I. B. Spielman, and G. K. Campbell, "Accurate Determination of Hubble Attenuation and Amplification in Expanding and Contracting Cold-Atom Universes," *Phys. Rev. Lett.* **128**, 090401 (2022).

[11] Maxime Jacquet, Malo Joly, Ferdinand Claude, Luca Giacomelli, Quentin Glorieux, Alberto Bramati, Iacopo Carusotto, and Elisabeth Giacobino, "Analogue quantum simulation of the Hawking effect in a polariton superfluid," *The European Physical Journal D* **76**, 152 (2022).

[12] Celia Viermann, Marius Sparn, Nikolas Liebster, Maurus Hans, Elinor Kath, Álvaro Parra-López, Mireia Tolosa-Simeón, Natalia Sánchez-Kuntz, Tobias Haas, Helmut Strobel, Stefan Floerchinger, and Markus K. Oberthaler, "Quantum field simulator for dynamics in curved spacetime," *Nature* **611**, 260–264 (2022).

[13] Kévin Falque, Adrià Delhom, Quentin Glorieux, Elisabeth Giacobino, Alberto Bramati, and Maxime J. Jacquet, "Polariton Fluids as Quantum Field Theory Simulators on Tailored Curved Spacetimes," *Phys. Rev. Lett.* **135**, 023401 (2025).

[14] Elliott H Lieb and Derek W Robinson, "The Finite Group Velocity of Quantum Spin Systems," *Commun. math. Phys* **28**, 251–257 (1972).

[15] F. D. M. Haldane, "Luttinger liquid theory of one-dimensional quantum fluids. I. Properties of the Luttinger model and their extension to the general 1D interacting spinless Fermi gas," *J. Phys. C* **14**, 2585–2609 (1981).

[16] Pasquale Calabrese and John Cardy, "Evolution of entanglement entropy in one-dimensional systems," *Journal of Statistical Mechanics: Theory and Experiment* **2005**, P04010 (2005).

[17] Pasquale Calabrese and John Cardy, "Time Dependence of Correlation Functions Following a Quantum Quench," *Phys. Rev. Lett.* **96**, 136801 (2006).

[18] Marc Cheneau, Peter Barmettler, Dario Poletti, Manuel Endres, Peter Schauß, Takeshi Fukuhara, Christian Gross, Immanuel Bloch, Corinna Kollath, and Stefan Kuhr, "Light-cone-like spreading of correlations in a quantum many-body system," *Nature* **481**, 484–487 (2012).

[19] T. Langen, R. Geiger, M. Kuhnert, B. Rauer, and J. Schmiedmayer, "Local emergence of thermal correlations in an isolated quantum many-body system," *Nature Physics* **9**, 640–643 (2013).

[20] P. Jurcevic, B. P. Lanyon, P. Hauke, C. Hempel, P. Zoller, R. Blatt, and C. F. Roos, "Quasiparticle engineering and entanglement propagation in a quantum many-body system," *Nature* **511**, 202–205 (2014).

[21] Mohammadamin Tajik, Marek Gluza, Nicolas Sebe, Philipp Schüttelkopf, Federica Cataldini, João Sabino, Frederik Møller, Si-Cong Ji, Sebastian Erne, Giacomo Guarneri, Spyros Sotiriadis, Jens Eisert, and Jörg Schmiedmayer, "Experimental observation of curved light-cones in a quantum field simulator," *Proceedings of the National Academy of Sciences* **120** (2023), 10.1073/pnas.2301287120.

[22] Yun-Hao Shi, Run-Qiu Yang, Zhongcheng Xiang, Zi-Yong Ge, Hao Li, Yong-Yi Wang, Kaixuan Huang, Ye Tian, Xiaohui Song, Dongning Zheng, Kai Xu, Rong-Gen Cai, and Heng Fan, "Quantum simulation of Hawking radiation and curved spacetime with a superconducting on-chip black hole," *Nature Communications* **14**, 3263 (2023).

[23] Carlos Sabín, "Digital quantum simulation of quantum gravitational entanglement with IBM quantum computers," *EPJ Quantum Technology* **10**, 4 (2023).

[24] Marco D. Maceda and Carlos Sabín, "Digital quantum simulation of cosmological particle creation with IBM quantum computers," *Scientific Reports* **15**, 3476 (2025).

[25] Yao-Yao Jiang, Chunqing Deng, Heng Fan, Bing-Yang Li, Luyan Sun, Xin-Sheng Tan, Weiting Wang, Guang-Ming Xue, Fei Yan, Hai-Feng Yu, Ying-Shan Zhang, Yu-Ran Zhang, and Chang-Ling Zou, "Advancements in superconducting quantum computing," *National Science Review* **12**, nwaf246 (2025).

[26] Benedikt Fauseweh, "Quantum many-body simulations on digital quantum computers: State-of-the-art and future challenges," *Nature Communications* **15**, 2123 (2024).

[27] Adam Smith, M. S. Kim, Frank Pollmann, and Johannes Knolle, "Simulating quantum many-body dynamics on a current digital quantum computer," *npj Quantum Information* **5**, 106 (2019).

[28] X. Mi, M. Sonner, M. Y. Niu, K. W. Lee, B. Foxen, R. Acharya, I. Aleiner, T. I. Andersen, F. Arute, K. Arya, A. Asfaw, J. Atalaya, J. C. Bardin, J. Basso, A. Bengtsson, G. Bortoli, A. Bourassa, L. Brill, M. Broughton, B. B. Buckley, D. A. Buell, B. Burkett, N. Bushnell, Z. Chen, B. Chiaro, R. Collins, P. Conner, W. Courtney, A. L. Crook, D. M. Debroy, S. Demura, A. Dunsworth, D. Eppens, C. Erickson, L. Faoro, E. Farhi, R. Fatemi, L. Flores, E. Forati, A. G. Fowler, W. Giang, C. Gidney, D. Gilboa, M. Giustina, A. G. Dau, J. A. Gross, S. Habegger, M. P. Harrigan, M. Hoffmann, S. Hong, T. Huang, A. Huff, W. J. Huggins, L. B. Ioffe, S. V. Isakov, J. Iveland, E. Jeffrey, Z. Jiang, C. Jones, D. Kafri, K. Kechedzhi, T. Khattar, S. Kim, A. Y. Kitaev, P. V. Klimov, A. R. Klots, A. N. Korotkov, F. Kostritsa, J. M. Kreikebaum, D. Landhuis, P. Laptev, K.-M. Lau, J. Lee, L. Laws, W. Liu, A. Locharla, O. Martin, J. R. McClean, M. McEwen, B. Meurer Costa, K. C. Miao, M. Mohseni, S. Montazeri, A. Morvan, E. Mount, W. Mruczkiewicz, O. Naaman, M. Neeley, C. Neill, M. Newman, T. E. O'Brien, A. Opremcak, A. Petukhov, R. Potter, C. Quintana, N. C. Rubin, N. Saei, D. Sank, K. Sankaragomathi, K. J. Satzinger, C. Schuster, M. J. Shearn, V. Shvarts, D. Strain, Y. Su, M. Szalay, G. Vidal,

B. Villalonga, C. Vollgraff-Heidweiller, T. White, Z. Yao, P. Yeh, J. Yoo, A. Zalcman, Y. Zhang, N. Zhu, H. Neven, D. Bacon, J. Hilton, E. Lucero, R. Babbush, S. Boixo, A. Megrant, Y. Chen, J. Kelly, V. Smelyanskiy, D. A. Abanin, and P. Roushan, “Noise-resilient edge modes on a chain of superconducting qubits,” *Science* **378**, 785–790 (2022).

[29] Roland C. Farrell, Marc Illa, Anthony N. Ciavarella, and Martin J. Savage, “Scalable Circuits for Preparing Ground States on Digital Quantum Computers: The Schwinger Model Vacuum on 100 Qubits,” *PRX Quantum* **5**, 020315 (2024).

[30] Alexander Miessen, Daniel J. Egger, Ivano Tavernelli, and Guglielmo Mazzola, “Benchmarking Digital Quantum Simulations Above Hundreds of Qubits Using Quantum Critical Dynamics,” *PRX Quantum* **5**, 040320 (2024).

[31] Tomoya Hayata, Kazuhiro Seki, and Seiji Yunoki, “Digital quantum simulation of many-body localization crossover in a disordered kicked Ising model,” (2025), arXiv:2510.01983 [quant-ph].

[32] Brendan Rhyno, Swarnadeep Majumder, Smitha Vishveshwara, and Khadijeh Najafi, “Quantum critical dynamics and emergent universality in decoherent digital quantum processors,” (2025), arXiv:2512.13143 [quant-ph].

[33] Nazlı Uğur Köylüoğlu, Swarnadeep Majumder, Mirko Amico, Sarah Mostame, Ewout van den Berg, M. A. Rajabpour, Zlatko Minev, and Khadijeh Najafi, “Measuring central charge on a universal quantum processor,” *Nature Communications* **17**, 305 (2026).

[34] Jérôme Dubail, Jean-Marie Stéphan, and Pasquale Calabrese, “Emergence of curved light-cones in a class of inhomogeneous Luttinger liquids,” *SciPost Phys.* **3**, 019 (2017).

[35] Jérôme Dubail, Jean-Marie Stéphan, Jacopo Viti, and Pasquale Calabrese, “Conformal field theory for inhomogeneous one-dimensional quantum systems: the example of non-interacting Fermi gases,” *SciPost Phys.* **2**, 002 (2017).

[36] Krzysztof Gawedzki, Edwin Langmann, and Per Moosavi, “Finite-Time Universality in Nonequilibrium CFT,” *Journal of Statistical Physics* **172**, 353–378 (2018).

[37] Paola Ruggiero, Pasquale Calabrese, Benjamin Doyon, and Jérôme Dubail, “Quantum Generalized Hydrodynamics,” *Phys. Rev. Lett.* **124**, 140603 (2020).

[38] Per Moosavi, “Inhomogeneous Conformal Field Theory Out of Equilibrium,” *Annales Henri Poincaré* **25**, 1083–1122 (2021).

[39] We note that in the most general case, inhomogeneous TLLs can have both spatially dependent velocity $v(x)$ and Luttinger parameter $K(x)$. In order for the model to retain conformal invariance, we choose to have only $v(x)$ to be inhomogeneous, which corresponds to having a spatially uniform anisotropy Δ in the XXZ model.

[40] Baptiste Bermond, Maxim Nikolaevich Chernodub, Adolfo G. Grushin, and David Carpentier, “Anomalous Luttinger equivalence between temperature and curved spacetime: From black holes to thermal quenches,” *SciPost Physics* **16** (2024), 10.21468/scipostphys.16.3.084.

[41] Ruihua Fan, Yingfei Gu, Ashvin Vishwanath, and Xueda Wen, “Emergent Spatial Structure and Entanglement Localization in Floquet Conformal Field Theory,” *Phys. Rev. X* **10**, 031036 (2020).

[42] John Cardy and Erik Tonni, “Entanglement Hamiltonians in two-dimensional conformal field theory,” *Journal of Statistical Mechanics: Theory and Experiment* **2016**, 123103 (2016).

[43] W. Zhu, Zhoushen Huang, Yin-Chen He, and Xueda Wen, “Entanglement Hamiltonian of Many-Body Dynamics in Strongly Correlated Systems,” *Phys. Rev. Lett.* **124**, 100605 (2020).

[44] Bastien Lapierre, Kenny Choo, Clément Tauber, Apoorv Tiwari, Titus Neupert, and Ramasubramanian Chitra, “Emergent black hole dynamics in critical Floquet systems,” *Phys. Rev. Res.* **2**, 023085 (2020).

[45] Bastien Lapierre and Per Moosavi, “Geometric approach to inhomogeneous Floquet systems,” *Phys. Rev. B* **103**, 224303 (2021).

[46] Viacheslav Kuzmin, Torsten V. Zache, Christian Kokail, Lorenzo Pastori, Alessio Celi, Mikhail Baranov, and Peter Zoller, “Probing Infinite Many-Body Quantum Systems with Finite-Size Quantum Simulators,” *PRX Quantum* **3**, 020304 (2022).

[47] Xueda Wen, Ruihua Fan, and Ashvin Vishwanath, “Floquet’s Refrigerator: Conformal Cooling in Driven Quantum Critical Systems,” (2022), arXiv:2211.00040 [cond-mat.str-el].

[48] Alexander Keesling, Ahmed Omran, Harry Levine, Hannes Bernien, Hannes Pichler, Soonwon Choi, Rhine Samajdar, Sylvain Schwartz, Pietro Silvi, Subir Sachdev, Peter Zoller, Manuel Endres, Markus Greiner, Vladan Vuletić, and Mikhail D. Lukin, “Quantum Kibble–Zurek mechanism and critical dynamics on a programmable Rydberg simulator,” *Nature* **568**, 207–211 (2019).

[49] Pasquale Calabrese and John Cardy, “Quantum quenches in 1+1 dimensional conformal field theories,” *Journal of Statistical Mechanics: Theory and Experiment* **2016**, 064003 (2016).

[50] See Supplemental Material (SM) for details regarding our quantum simulations and error analysis, along with further experimental results for the local magnetization dynamics, ballistic spreading in the XXZ chain, and connected correlations from an initial Néel state.

[51] Farrokh Vatan and Colin Williams, “Optimal quantum circuits for general two-qubit gates,” *Phys. Rev. A* **69**, 032315 (2004).

[52] Nathan Keenan, Niall F. Robertson, Tara Murphy, Sergiy Zhuk, and John Goold, “Evidence of Kardar–Parisi–Zhang scaling on a digital quantum simulator,” *npj Quantum Information* **9**, 72 (2023).

[53] Peter Barmettler, Matthias Punk, Vladimir Gritsev, Eugene Demler, and Ehud Altman, “Quantum quenches in the anisotropic spin-1/2 Heisenberg chain: different approaches to many-body dynamics far from equilibrium,” *New Journal of Physics* **12**, 055017 (2010).

[54] Paul Niklas Jepsen, Jesse Amato-Grill, Ivana Dimitrova, Wen Wei Ho, Eugene Demler, and Wolfgang Ketterle, “Spin transport in a tunable Heisenberg model realized with ultracold atoms,” *Nature* **588**, 403–407 (2020).

[55] T. Giamarchi, *Quantum Physics in One Dimension* (Oxford University Press, Oxford, 2003).

[56] Tomaž Prosen and Marko Žnidarič, “Matrix product simulations of non-equilibrium steady states of quantum spin chains,” *Journal of Statistical Mechanics: Theory and Experiment* **2009**, P02035 (2009).

[57] Petr O. Fedichev and Uwe R. Fischer, ““Cosmological”

quasiparticle production in harmonically trapped superfluid gases,” *Phys. Rev. A* **69**, 033602 (2004).

[58] Piyush Jain, Silke Weinfurtner, Matt Visser, and C. W. Gardiner, “Analog model of a Friedmann-Robertson-Walker universe in Bose-Einstein condensates: Application of the classical field method,” *Phys. Rev. A* **76**, 033616 (2007).

[59] Angus Prain, Serena Fagnocchi, and Stefano Liberati, “Analogue cosmological particle creation: Quantum correlations in expanding Bose-Einstein condensates,” *Phys. Rev. D* **82**, 105018 (2010).

[60] Jörg Schmiedmayer and Jürgen Berges, “Cold Atom Cosmology,” *Science* **341**, 1188–1189 (2013).

[61] Jeff Steinhauer, Murad Abuzarli, Tangui Aladjidi, Tom Bienaimé, Clara Piekarski, Wei Liu, Elisabeth Giacobino, Alberto Bramati, and Quentin Glorieux, “Analogue cosmological particle creation in an ultracold quantum fluid of light,” *Nature Communications* **13**, 2890 (2022).

[62] Mireia Tolosa-Simeón, Álvaro Parra-López, Natalia Sánchez-Kuntz, Tobias Haas, Celia Viermann, Marius Sparn, Nikolas Liebster, Maurus Hans, Elinor Kath, Helmut Strobel, Markus K. Oberthaler, and Stefan Floerchinger, “Curved and expanding spacetime geometries in Bose-Einstein condensates,” *Phys. Rev. A* **106**, 033313 (2022).

[63] Anshuman Bhardwaj, Ivan Agullo, Dimitrios Kranas, Justin H. Wilson, and Daniel E. Sheehy, “Entanglement in an expanding toroidal Bose-Einstein condensate,” *Phys. Rev. A* **109**, 013305 (2024).

[64] L. J. Garay, J. R. Anglin, J. I. Cirac, and P. Zoller, “Sonic Analog of Gravitational Black Holes in Bose-Einstein Condensates,” *Phys. Rev. Lett.* **85**, 4643–4647 (2000).

[65] Mário Novello, Matt Visser, and Grigory E Volovik, *Artificial Black Holes* (World Scientific, 2002).

[66] Matt Visser, Carlos Barceló, and Stefano Liberati, “Analogue Models of and for Gravity,” *General Relativity and Gravitation* **34**, 1719–1734 (2002).

[67] Jeff Steinhauer, “Observation of quantum Hawking radiation and its entanglement in an analogue black hole,” *Nature Physics* **12**, 959–965 (2016).

[68] Carlos Barceló, Stefano Liberati, and Matt Visser, “Analogue Gravity,” *Living Reviews in Relativity* **14**, 1–159 (2011).

[69] Grigory E. Volovik, *The Universe in a Helium Droplet* (Oxford University Press, 2009).

[70] Brian Swingle, “Unscrambling the physics of out-of-time-order correlators,” *Nature Physics* **14**, 988–990 (2018).

[71] Brian Swingle, Gregory Bentsen, Monika Schleier-Smith, and Patrick Hayden, “Measuring the scrambling of quantum information,” *Phys. Rev. A* **94**, 040302 (2016).

[72] Ceren B. Dağ and L.-M. Duan, “Detection of out-of-time-order correlators and information scrambling in cold atoms: Ladder-XX model,” *Phys. Rev. A* **99**, 052322 (2019).

[73] Bastien Lapierre, Tokiro Numasawa, Titus Neupert, and Shinsei Ryu, “Floquet engineered inhomogeneous quantum chaos in critical systems,” *Phys. Rev. B* **112**, 104317 (2025).

[74] Denis Bernard and Pierre Le Doussal, “Entanglement entropy growth in stochastic conformal field theory and the KPZ class,” *Europhysics Letters* **131**, 10007 (2020).

[75] Jonathan Oppenheim, “Postquantum Theory of Classical Gravity,” *Physical Review X* **13**, 041040 (2023).

[76] Ahmed Almheiri and Joseph Polchinski, “Models of AdS_2 backreaction and holography,” *Journal of High Energy Physics* **2015**, 1–23 (2015).

[77] Philip K Schwartz and Domenico Giulini, “Post-Newtonian corrections to Schrödinger equations from semiclassical gravity,” *Classical and Quantum Gravity* **36**, 095016 (2019).

[78] Michael A Nielsen and Isaac L Chuang, *Quantum Computation and Quantum Information* (Cambridge University Press, 2001).

[79] H. F. Trotter, “On the Product of Semi-Groups of Operators,” *Proceedings of the American Mathematical Society* **10**, 545–551 (1959).

[80] Masuo Suzuki, “General Decomposition Theory of Ordered Exponentials,” *Proceedings of the Japan Academy, Series B* **69**, 161–166 (1993).

Supplementary Material for “Observing quantum many-body dynamics in emergent curved spacetime using programmable quantum processors”

Brendan Rhyno^{1,2}, Bastien Lapierre^{3,4}, Smitha Vishveshwara¹, Khadijeh Najafi^{5,6}, and Ramasubramanian Chitra⁷

¹Department of Physics, University of Illinois at Urbana-Champaign, Urbana, Illinois 61801, USA

²Institute of Quantum Optics, Leibniz Universität Hannover, Welfengarten 1, 30167 Hannover, Germany

³Department of Physics, Princeton University, Princeton, New Jersey, 08544, USA

⁴Philippe Meyer Institute, Physics Department, École Normale Supérieure (ENS), Université PSL, 24 rue Lhomond, F-75231 Paris, France

⁵IBM Quantum, IBM T.J. Watson Research Center, Yorktown Heights, 10598, USA

⁶MIT-IBM Watson AI Lab, Cambridge MA, 02142, USA

⁷Institute for Theoretical Physics, ETH Zurich, Wolfgang-Pauli-Str. 27, CH-8093 Zurich, Switzerland

(Dated: February 18, 2026)

This Supplemental Material comprises several appendices containing technical details and additional data that support the results presented in the main text. Appendix A details the implementation of the inhomogeneous XXZ spin chain on IBM quantum processors. Appendix B details the error analysis performed on measured quantities. Appendix C presents further data on the local magnetization, including results obtained in the absence of deformation or in the non-interacting limit. Appendix D provides additional data on the ballistic spreading of excitations. Finally, Appendix E reports comprehensive quantum-simulation results for the two-point correlators.

Appendix A: Simulating spin chain dynamics using IBM quantum computers

In this appendix, we provide details on how initial states are prepared, time evolution with the XXZ model is performed, and correlators are extracted using IBM Quantum hardware.

Initial state preparation: By default, the N -qubit quantum circuits that we study with IBM Quantum hardware are initialized in the all-up state $|\uparrow \dots \uparrow\rangle = |\uparrow\rangle \otimes \dots \otimes |\uparrow\rangle$. In this work, we consider initial product states of the form

$$|j_1, j_2, \dots\rangle = |\uparrow \dots \downarrow \dots \downarrow \dots \uparrow\rangle, \quad (A1)$$

where the spins at the sites j_1, j_2, \dots are down, with the rest being up. We will be particularly interested in the Néel state, $|\uparrow\downarrow\uparrow\downarrow\dots\uparrow\downarrow\rangle$, which consists of alternating up and down spins. The initial-state preparation consists of a single gate layer to flip each spin at the desired sites by applying the Pauli-X gate,

$$|\downarrow\rangle = |\uparrow\rangle \xrightarrow{\quad X \quad} . \quad (A2)$$

Time evolution: For a static Hamiltonian, unitary time evolution is achieved by acting the operator $U(t) = e^{-itH}$ on the initial state $|\Psi_0\rangle$. Here, we simulate dynamics in discrete steps of constant duration δt . Namely, to evolve the system to time $t_s = s\delta t$ with s a nonnegative integer, we apply the operator

$$U(s\delta t) = \underbrace{e^{-i\delta t H} \dots e^{-i\delta t H}}_{s \text{ times}}. \quad (A3)$$

To simulate time evolution of the inhomogeneous XXZ model, Eq. (2), we utilize the optimal decomposition with regard to two qubit gates in [27, 51, 52]:

$$N_{j_1, j_2}(\alpha, \beta, \gamma) \equiv e^{i(\alpha\sigma_{j_1}^x\sigma_{j_2}^x + \beta\sigma_{j_1}^y\sigma_{j_2}^y + \gamma\sigma_{j_1}^z\sigma_{j_2}^z)} = e^{i\pi/4} \cdot \begin{array}{c} j_1 \xrightarrow{\oplus} R_Z\left(\frac{\pi}{2} - 2\gamma\right) \xrightarrow{\bullet} \dots \xrightarrow{\oplus} R_Z\left(\frac{\pi}{2}\right) \\ j_2 \xrightarrow{R_Z\left(-\frac{\pi}{2}\right)} \dots \xrightarrow{\bullet} R_Y\left(2\alpha - \frac{\pi}{2}\right) \xrightarrow{\oplus} R_Y\left(\frac{\pi}{2} - 2\beta\right) \xrightarrow{\bullet} \dots \end{array}, \quad (A4)$$

where the top (bottom) wire refers to qubit j_1 (j_2). The single qubit gates “ $R_\alpha(\theta)$ ” rotate a qubit about the α -axis by angle θ . The vertical connected wires represent controlled-X gates or “CNOT” gates where the solid dot refers to the control qubit and the circled plus refers to the target qubit [78]. There is a global phase factor that appears on all qubits and can be safely disregarded [51]. Also note that using the top wire for qubit j_1 and the bottom wire for qubit j_2 was an arbitrary choice as the circuit is invariant under swapping the two qubits [27].

For each time step, we approximate the operator $e^{-i\delta t H}$ for the Hamiltonian in Eq. (2) using a first-order Suzuki-Trotter decomposition [79, 80]:

$$e^{-i\delta t(A+B)} = e^{-i\delta tA}e^{-i\delta tB} + \mathcal{O}(\delta t^2). \quad (\text{A5})$$

A first-order decomposition is done as higher-order Trotter breakups introduce increased gate depth [27]. One can write the inhomogeneous XXZ Hamiltonian as $H = \sum_{j=1}^{N-1} h_j$ where $h_j \equiv v_j [\sigma_j^x \sigma_{j+1}^x + \sigma_j^y \sigma_{j+1}^y + \Delta \sigma_j^z \sigma_{j+1}^z]$ is a local energy density. Importantly, these local operators do not commute at adjacent sites:

$$[h_{j_1}, h_{j_2}] \neq 0, \text{ if } j_2 = j_1 \pm 1. \quad (\text{A6})$$

Assuming δt is sufficiently small, we use the Suzuki-Trotter decomposition in Eq. (A5) by setting $A \equiv \sum_{j \in \text{even}} h_j$ and $B \equiv \sum_{j \in \text{odd}} h_j$ [52]. These operators do not commute, $[A, B] \neq 0$, but each local operator within A commutes (similarly for B). This allows us to write the Trotterized operator using products of the unitary in Eq. (A4). In particular, a single Trotterized time-step forward is achieved with:

$$e^{-i\delta t H} \approx \prod_{j \in \text{even}} N_{j,j+1}(-\delta t v_j, -\delta t v_j, -\delta t v_j \Delta) \prod_{j \in \text{odd}} N_{j,j+1}(-\delta t v_j, -\delta t v_j, -\delta t v_j \Delta)$$


$\Delta = 0$ case: To simulate a time step forward with the inhomogeneous XX model, one could use the previous result in Eq. (A7) and simply set $\Delta = 0$. However, the 3 CNOT gates involved in each application of Eq. (A4) is not optimal. Indeed, for $\Delta = 0$, one can reduce the number of CNOT gates from 3 down to 2 [27]. Here, we use the circuit in [27] to implement the following XZ unitary:

$$N_{j_1, j_2}(\alpha, 0, \gamma) = e^{i(\alpha \sigma_{j_1}^x \sigma_{j_2}^x + \gamma \sigma_{j_1}^z \sigma_{j_2}^z)} = \begin{array}{c} \text{Quantum Circuit Diagram} \\ \text{Two qubits } j_1 \text{ and } j_2. \\ \text{Top wire } j_1: \text{Control for } R_Z(-2\gamma) \text{ and } R_X(-2\alpha). \\ \text{Bottom wire } j_2: \text{Control for } R_X(-2\alpha). \end{array} \quad (A8)$$

Because this circuit realizes Ising XX and ZZ terms, instead of the desired XX and YY terms, we rotate all qubits 90 degrees about the x -axis:

$$N_{j_1, j_2}(\alpha, \beta, 0) = e^{i(\alpha \sigma_{j_1}^x \sigma_{j_2}^x + \beta \sigma_{j_1}^y \sigma_{j_2}^y)} = \begin{array}{c} j_1 \xrightarrow{R_X(\pi/2)} \oplus \xrightarrow{R_Z(-2\beta)} \oplus \xrightarrow{R_X(-\pi/2)} \\ j_2 \xrightarrow{R_X(\pi/2)} \bullet \xrightarrow{R_X(-2\alpha)} \bullet \xrightarrow{R_X(-\pi/2)} \end{array} . \quad (A9)$$

One can now proceed to construct a circuit that implements the (Trotterized) time-step forward in the exact same manner as we did for the XXZ model. Simply use the circuit shown in Eq. (A7), but substitute Eq. (A9) for the XY unitary circuit. However, there is another simplification that can be made. When substituting Eq. (A9) into Eq. (A7), a great deal of cancellation occurs between the X-rotation gates. Between the even and odd sub-layers of each Trotter layer, and also with the application of each additional Trotter layer, the X-rotation gates encounter their inverse. Hence, we only apply a single layer of X-rotation gates at the start of the time evolution and then apply its inverse at the very end.

Projective measurements: The Qiskit Runtime Sampler primitive allows one to submit their quantum circuits through the IBM cloud to be run on backend quantum hardware. By default, the Sampler primitive measures these circuits in the computational basis ($|0\rangle = |\uparrow\rangle$ and $|1\rangle = |\downarrow\rangle$) for a specified number of shots and returns the number of counts (i.e. the number of times a given configuration was observed). From the probability of a configuration occurring, one can then construct the expectation values of various equal-time Pauli-Z operators (e.g. $\langle \sigma_j^z(t) \rangle = \sum_{\{n_i=0,1\}} p_{\{n_i\}}(t)(1-2n_j)$ where $\{n_i\}$ is a computational basis configuration and $p_{\{n_i\}}(t)$ the probability of measuring the configuration at time t). To extract these expectation values for multiple time-steps $s = 0, 1, 2, \dots, P$ ($s = 0$ corresponds to measurements of the initial state), one would submit the following batch of circuits to the Sampler primitive:

$$\begin{aligned}
 s = 0 : |\Psi_0\rangle &\equiv \text{gate} \\
 s = 1 : |\Psi_0\rangle &\equiv e^{-i\delta t H} \text{gate} \\
 s = 2 : |\Psi_0\rangle &\equiv e^{-i\delta t H} \text{gate} \equiv e^{-i\delta t H} \text{gate} \\
 &\vdots \\
 s = P : |\Psi_0\rangle &\equiv e^{-i\delta t H} \equiv \dots \equiv e^{-i\delta t H} \equiv \dots \equiv e^{-i\delta t H} \text{gate} , \tag{A10}
 \end{aligned}$$

where each unitary is replaced with the previously discussed Trotter decomposition.

Appendix B: Error analysis

When displayed, the error bars reported on the measurements of an operator O are standard errors calculated using $\delta_{\langle O \rangle} = \sqrt{\text{Var}(O)/\text{shots}}$ where $\text{Var}(O) = \langle O^2 \rangle - \langle O \rangle^2$ is the measured variance in the operator and shots ($= 2^{14}$) is the number of measurements used in the experiment. For the local magnetization along the z -axis, $M_j^z(t) = \langle \sigma_j^z(t) \rangle$, one finds

$$\delta_{M_j^z(t)} = \sqrt{\frac{1 - \langle \sigma_j^z(t) \rangle^2}{\text{shots}}} . \tag{B1}$$

For the equal-time connected spin-spin correlation function, $C_{ij}^{zz}(t) = \langle \sigma_i^z(t) \sigma_j^z(t) - M_i^z(t) M_j^z(t) \rangle$, one finds

$$\delta_{C_{ij}^{zz}(t)} = \sqrt{\frac{1 - \langle \sigma_i^z(t) \sigma_j^z(t) \rangle^2}{\text{shots}}} . \tag{B2}$$

In both cases, the maximum standard error on these local correlation functions is $\sqrt{1/\text{shots}} = 0.0078125$ which is of the order 10^{-2} .

Appendix C: Local magnetization dynamics

In this appendix, we provide further data on the time evolution of the magnetization for a system initialized in a Néel state, both for uniform and inhomogeneous XXZ quenches.

1. Uniform XXZ chain

Our primary focus lies on effective curved-spacetime dynamics induced by spatial deformation. For completeness, however, we also report results for magnetization dynamics in the uniform XXZ chain ($v_j \equiv 1$). In this case, as was both analytically and numerically studied in [53], one expects damped oscillations of the magnetization in the gapless regime ($|\Delta| < 1$) and no oscillations in the gapped regime ($|\Delta| > 1$). We confirm this behavior in Fig. S1 by studying the time evolution of the staggered magnetization, defined as

$$M_s^z(t) = \frac{1}{N-2n} \sum_{j=n+1}^{N-n} (-1)^{j-1} M_j^z(t), \quad (\text{C1})$$

where the threshold $n = 9$ was chosen to suppress the finite-size effects associated with open boundary conditions. In particular, we find that the oscillation frequency does not directly depend on the anisotropy Δ within the gapless

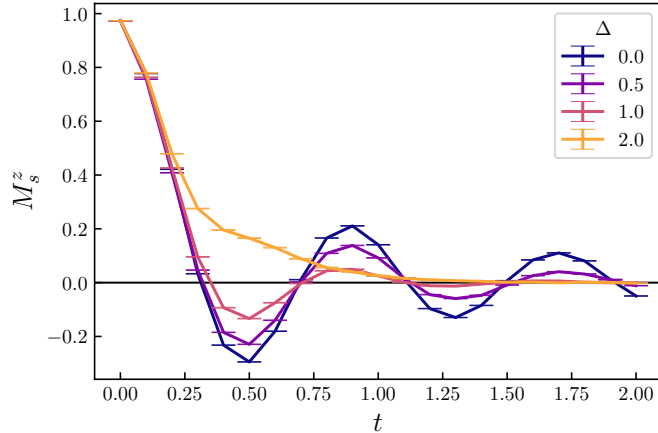


Figure S1. Time evolution of the staggered magnetization for a quench with the uniform XXZ chain (with $N = 80$ qubits) initialized in a Néel state, with different values of the anisotropy $\Delta = 0, 1/2, 1, 2$. Damped oscillations appear in the gapless phase of the XXZ model, while they are clearly absent in the gapped phase. The error bars are standard errors, given by $\delta_{M_s^z(t)} = \sqrt{\sum_{ij=n+1}^{N-n} f_i f_j C_{ij}^{zz}(t)}/\text{shots}$ where $f_j = (-1)^{j-1}/(N-2n)$, and $C_{ij}^{zz}(t)$ is the measured equal-time connected spin-spin correlation function.

regime, as expected, while increasing Δ leads to a faster decay of the magnetization. These results provide an experimental verification of the tensor network calculations in Ref. [53].

2. Deformed XX chain ($\Delta = 0$)

In this section, we provide data for the inhomogeneous non-interacting limit of the XXZ model, which we refer to as the inhomogeneous XX model. This spin model can be mapped through a Jordan-Wigner transformation to a free-fermionic model of the form

$$H_{\text{free}} = 2J \sum_{j=1}^{N-1} v_j (c_{j+1}^\dagger c_j + h.c.). \quad (\text{C2})$$

Using exact diagonalization, we compute the local magnetization $\langle \sigma_j^z(t) \rangle = 1 - 2\langle n_j(t) \rangle$, starting from the product state $|0101 \cdots 01\rangle$. Similar to the uniform case $v_j \equiv 1$, the dynamics of $\langle \sigma_j^z(t) \rangle$ displays robust oscillations in this non-interacting setting. While in the uniform case the frequency of the oscillations is set by J , we find that in the inhomogeneous case the frequency depends on space through $\omega_j \sim Jv_j$. This behavior is illustrated in Fig. S2, where the local frequency ω_j is explicitly compared to the deformation profile v_j . This numerical calculation shows that the local deformation profile completely determines the oscillatory dynamics of the local magnetization in the noninteracting limit.

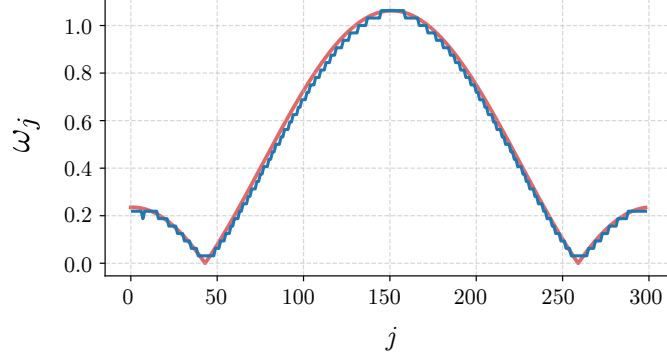


Figure S2. Numerical comparison between the spatially-dependent frequency ω_j in the oscillations of $\langle \sigma_j^z(t) \rangle$ after a quench with (C2) (blue) with the absolute value deformation profile given by (4) (red), for a system size of $N = 300$. As is manifest from the plot, the frequency follows the local deformation profile in the thermodynamic limit.

We now present data of the magnetization dynamics for the XX chain, as shown in Fig. S3. Similarly to the interacting setting, we observe a clear spatial dependence of the periodicity that reflects the deformation profile. We note that the oscillations are more robust compared to the interacting gapless setting $\Delta \neq 0$ (shown in the main text in Fig. 4(a-c)), as expected.

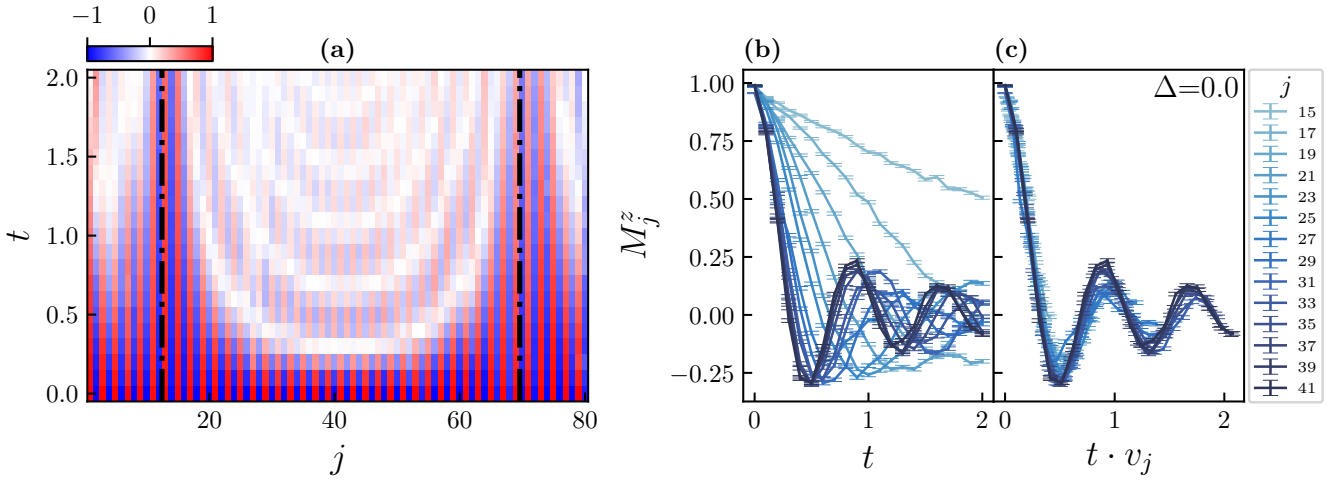


Figure S3. (a) data for the magnetization dynamics starting from a Néel state with $N = 80$ qubits, evolving with the noninteracting inhomogeneous spin chain, $\Delta = 0$. (b) Damped oscillations at different initial positions reveal a strong position dependence of the frequency. (c) Collapse of the magnetization curves after rescaling the time axis by the spatial deformation.

Appendix D: Ballistic spreading in the XXZ chain ($\Delta = 1/2$)

In this section, we discuss the experimental procedure to extract the unequal-time spin-spin correlation function $G_{ji}^{zz}(t, 0) = \langle \sigma_j^z(t) \sigma_i^z(0) \rangle$ along with the background subtraction method used to generate Fig. 5 in the main text. Due to the form of the initial states considered in this work, Eq. (A1), the unequal-time spin-spin correlation function is related to the local magnetization by $G_{ji}^{zz}(t, 0) = M_j^z(t) M_i^z(0)$ (assuming perfect initial state preparation). Furthermore, one should observe $M_i^z(0) = \pm 1$, which simply contributes an overall sign. Hence, moving forward, we focus only on $M_j^z(t)$ as an effective proxy for $G_{ji}^{zz}(t, 0)$. Using $N = 80$ qubits on `ibm_fez`, we consider various initial states time evolving under the $\Delta = 1/2$ XXZ Hamiltonian for $s = 0, 1, 2, \dots, 20$ Trotterized steps, with both uniform couplings and deformed couplings given by the profile in Eq. (4). Upon reaching the discrete time $t_s = s\delta t$ with $\delta t = 0.1$, we measure the final state in the computational basis using 2^{14} shots. From the shot data, we extract

the local z -component of the magnetization. For both uniform and deformed Hamiltonians, we consider the following initial states, $|\Psi_0\rangle$:

$$|\uparrow \dots \uparrow\rangle, \quad |20, 30\rangle = \sigma_{20}^x \sigma_{30}^x |\uparrow \dots \uparrow\rangle, \quad |20\rangle = \sigma_{20}^x |\uparrow \dots \uparrow\rangle, \quad |30\rangle = \sigma_{30}^x |\uparrow \dots \uparrow\rangle. \quad (\text{D1})$$

Note: In order for the measured observables to experience similar hardware noise across all initial states, these jobs were submitted in quick succession. In the specific case of the deformed XXZ chain with the all-up initial state, $|\Psi_0\rangle = |\uparrow \dots \uparrow\rangle$, the $s = 14$ Trotter step job submission failed to run. Due to the background subtraction method to be outlined in what follows, and without running all simulations again, we opted to approximate the $s = 14$ correlators for this particular run using $G(t = 14\delta t) \approx \frac{1}{2}[G(t = 13\delta t) + G(t = 15\delta t)]$ where $G(t)$ represents an arbitrary equal-time correlation function.

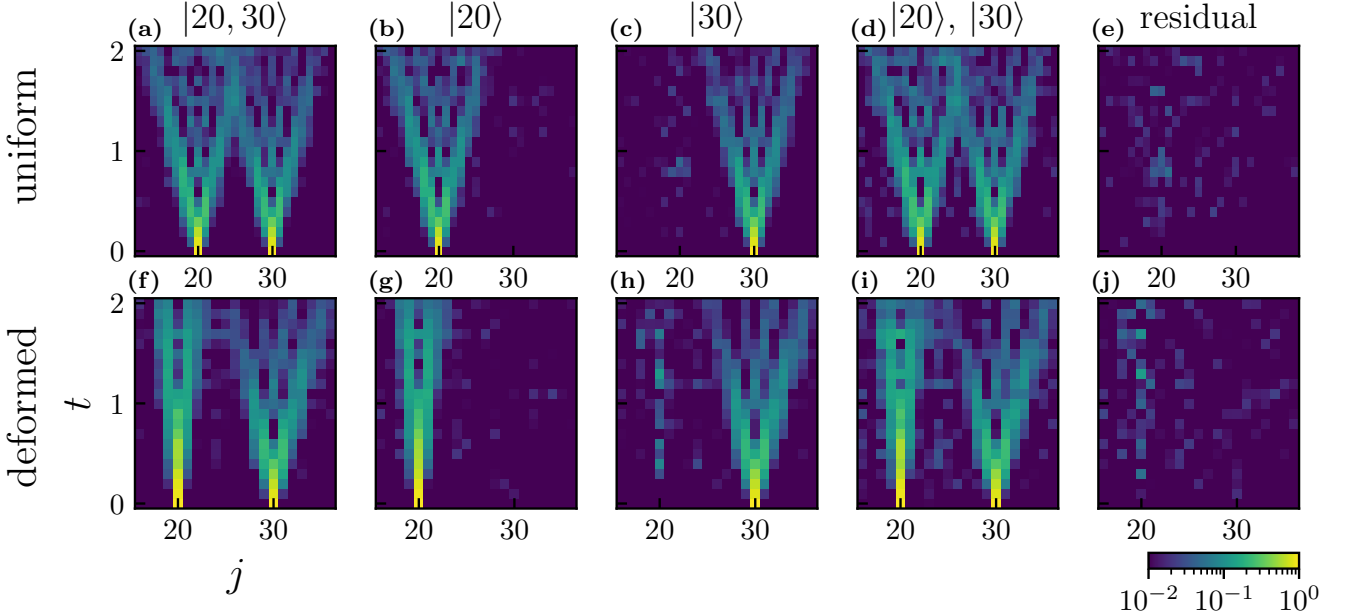


Figure S4. (a-e): Local magnetization data generated from quantum simulations of the uniform $\Delta = 1/2$ XXZ chain performed on `ibm_fez` with $N = 80$ qubits. (f-j): Quantum simulations using the same parameters as the top row, except now with the deformation profile in Eq. (4). Columns 1, 2, and 3 correspond to the background-subtracted local magnetization, Eq. (D2), for initial states $|\Psi_0\rangle = |20, 30\rangle, |20\rangle, |30\rangle$ respectively. Column 4 shows the results of adding together the local magnetization produced from initial states $|\Psi_0\rangle = |20\rangle$ and $|\Psi_0\rangle = |30\rangle$ (including the background subtraction), Eq. (D3). Column 5 displays the absolute value of the difference between the data sets in column 1 and 4. Consistent log scale color maps are used throughout whose minimum value, 10^{-2} , was chosen as it is on the same order of magnitude as the standard error in the local magnetization.

For the $\Delta = 1/2$ XXZ chain, we expect correlations to spread ballistically, as they are carried by effectively non-interacting gapless quasiparticles. To probe this, we consider the behavior of the local magnetization generated from two distinct protocols. In the first protocol, we measure the local magnetization in the case where the initial state has 2 spins pointing down at sites 20 and 30, $M_j^z(t; |20, 30\rangle)$. In the second protocol, we measure the local magnetization in the case where the initial state has a single down spin at site 20, $M_j^z(t; |20\rangle)$, and also perform the same experiments for an initial state that has a single down spin at site 30, $M_j^z(t; |30\rangle)$. We then add these correlators, $M_j^z(t; |20\rangle) + M_j^z(t; |30\rangle)$.

For information that spreads ballistically, we expect the same results from the two protocols. However, because of the noise in the quantum hardware, one should expect that the additive nature of the second protocol will amplify systematic noise. To mitigate this, we perform a background subtraction using the local magnetization measured in the case where the initial state has all the spins pointing up, $M_j^z(t; |\uparrow \dots \uparrow\rangle)$. Because the all-up state $|\uparrow \dots \uparrow\rangle$ is an eigenstate of the XXZ Hamiltonian, in noise-free hardware the magnetization would always be equal to 1. With this in mind, in the first, second, and third columns of Fig. S4, we show the background-subtracted local magnetization for the initial states of interest:

$$\frac{1}{2} |M_j^z(t; |\Psi_0\rangle) - M_j^z(t; |\uparrow \dots \uparrow\rangle)|, \quad (\text{D2})$$

where $|\Psi_0\rangle = |20, 30\rangle, |20\rangle, |30\rangle$ and the range of the function is the unit interval $[0, 1]$. For both uniform and deformed chains, we have zoomed in on the combined causal regions of the excitations emitted at sites 20 and 30. In the fourth column of Fig. S4, we show the background-subtracted local magnetization when the $|20\rangle$ and $|30\rangle$ initial state experimental runs are added together:

$$\frac{1}{2} |M_j^z(t; |20\rangle) + M_j^z(t; |30\rangle) - 2M_j^z(t; |\uparrow \dots \uparrow\rangle)|. \quad (\text{D3})$$

Finally, in the last column of Fig. S4, we quantify the similarity of the two protocols (Eq. (D2) for $|\Psi_0\rangle = |20, 30\rangle$ and Eq. (D3)) by displaying the absolute value of the difference between the two data sets. In both uniform and deformed chains, we see excellent agreement between the two approaches in the causal region, with the strongest deviations occurring near site 20.

Appendix E: Supplementary data for the connected two-point correlation function

On the following pages, we provide additional two-point correlation function data for the case that a $N = 80$ qubit chain, initialized in a Néel state, is quenched according to the XXZ Hamiltonian, Eq. (2). In Fig. S5, expanding on the data shown in Fig. 2 of the main text, we show the dynamics generated by both uniform and deformed Hamiltonians for the case that $\Delta = 1/2$. In Fig. S6, expanding on the data shown in Fig. 3 of the main text, we show the dynamics generated by the deformed Hamiltonian for different values of the anisotropy. For all inhomogeneous XXZ chains, the deformation profile is given by Eq. (4) with $j_* = N/7$.

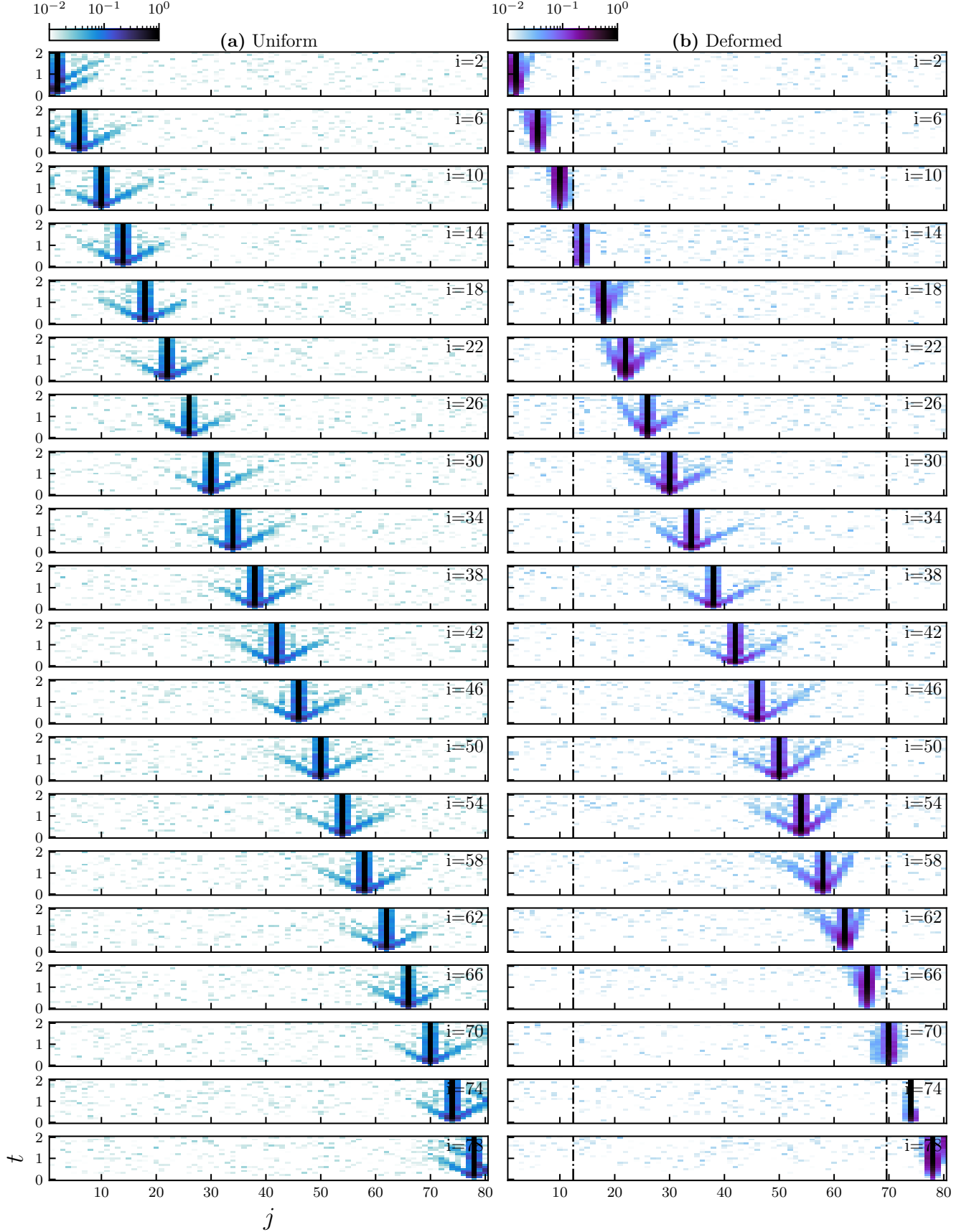


Figure S5. Digital quantum simulations of the $\Delta = 1/2$ XXZ chain using $N = 80$ qubits initialized in a Néel state. (a) Uniform chain simulation run on `ibm_fez` on 2025-05-30. (b) Deformed chain simulation run on `ibm_marrakesh` on 2025-05-30. The deformation profile in (b) is given by Eq. (4) and Rindler horizons located at $j_* + 1$ and $N + 1 - j_*$ ($j_* = N/7$) are indicated with black dash-dot vertical lines. Here we show $|C_{ij}^{zz}(t)|$ data for every 4th site in the chain.

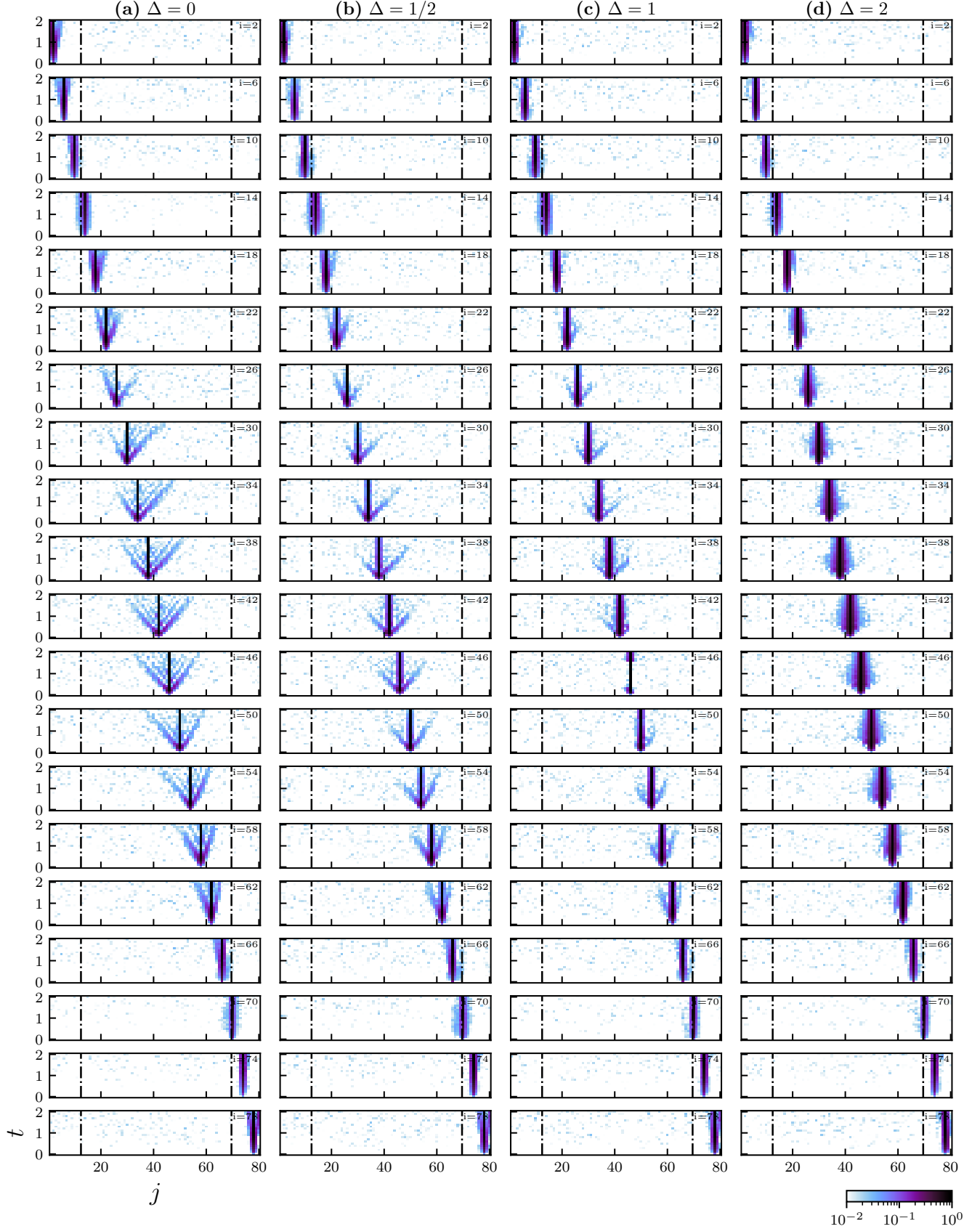


Figure S6. Digital quantum simulations of the inhomogeneous XXZ chain using $N = 80$ qubits initialized in a Néel state and various anisotropies. All simulation were run on `ibm_fez` on 2025-05-30. Columns (a)-to-(d) correspond to simulations using $\Delta = 0, 1/2, 1, 2$ respectively. The deformation profile is given by Eq. (4) and Rindler horizons located at $j_* + 1$ and $N + 1 - j_*$ ($j_* = N/7$) are indicated with black dash-dot vertical lines. Here we show $|C_{ij}^{zz}(t)|$ data for every 4th site in the chain.